Journal of ELECTRONIC MATERIALS, Vol. 49, No. 9, 2020
https://doi.org/10.1007/s11664-020-08187-7
© 2020 The Minerals, Metals & Materials Society

TOPICAL COLLECTION: 18TH CONFERENCE ON DEFECTS (DRIP XVIII)

Microstructure of Stacking Fault Complex/Carrot Defects at Interface Between 4H-SiC Epitaxial Layers and Substrates

HIDEKI SAKO,[1,3,4] KENJI KOBAYASHI,[2] KENTARO OHIRA,[2] and TOSHIYUKI ISSHIKI[3]

1.—Toray Research Center, Inc., 3-7, Sonoyama 3, Otsu, Shiga 520-8567, Japan. 2.—Hitachi High-Technologies Corp., Ichige, Hitachinaka, Ibaraki 312-8504, Japan. 3.—Kyoto Institute of Technology, Matsugasaki, Sakyo-ku, Kyoto 606-8585, Japan. 4.—e-mail: Hideki_Sako@trc.toray.co.jp

A carrot defect with a shallow pit has been detected in a 4H-SiC epitaxial wafer using mirror projection electron microscopy inspection. The origin of the carrot defect and the microstructure of the conversion point at the interface between the epitaxial layer and the substrate were investigated using transmission electron microscopy and high-resolution scanning transmission electron microscopy. We found that two types of threading edge dislocations (TEDs) in the substrate, with $\boldsymbol{b} = 1/3[\bar{2}110]$ and $\boldsymbol{b} = 1/3[\bar{1}\bar{1}20]$, generated the carrot defect with a shallow pit in the epitaxial layer. The two TEDs converted to basal plane dislocations (BPDs) at the conversion point. Furthermore, one of the two BPDs led to the pair generation of a threading dislocation running to the epi surface and four partial dislocations propagating on each basal plane. The other BPD joined one of the four partial dislocations at the conversion point; this merged dislocation was assumed to cause a prismatic stacking fault.

Key words: 4H-SiC, carrot defect, stacking fault complex, dislocation, Burgers vector, transmission electron microscopy

INTRODUCTION

4H-SiC is a promising material for high-power, high-temperature, and high-voltage devices because of its wide bandgap, high electric breakdown field, and high thermal conductivity. High-quality 4H-SiC epitaxial growth, which is indispensable to ensure high performance of devices, has been realized using some key technologies, such as "step-controlled epitaxy."[1] However, 4H-SiC epitaxial wafers still contain a variety of extended defects with surface roughness, which is detrimental to the performance of SiC power devices; nevertheless, the crystal growth processes have improved. Reducing the number of extended defects in the epitaxial layer is an important issue in the fabrication of large-area devices. Stacking fault complexes, also termed carrot defects, are one of the aforementioned extended defects. Carrot defects have been reported to negatively affect the reliability and yield of SiC metal–oxide–semiconductor field-effect transistor devices.[2] A carrot defect consists of a prismatic stacking fault (PSF) with surface roughness and a Frank-type basal plane stacking fault (Frank-type SF) with a stair-rod dislocation at the crossover,[3] as shown in Fig. 1. The formation mechanism and origins of carrot defects have been examined in several studies.[3–5] However, few studies have tried to characterize the microstructure of the conversion point from its origin, such as threading screw dislocation (TSD) or threading mix dislocation (TMD), to the carrot defects at the interface between the 4H-SiC epitaxial layer and substrate. We detected a carrot defect with a shallow pit on the upstream side by using mirror projection electron

(Received December 16, 2019; accepted April 29, 2020; published online May 13, 2020)

microscopy (MPJ).[6,7] In this study, we aimed to analyze the microstructure of the conversion point of the carrot defect at the interface between the epitaxial layer and the substrate by using transmission electron microscopy (TEM) and high-resolution scanning transmission electron microscopy (STEM).

EXPERIMENTAL PROCEDURES

The sample used in this study was a commercially available, four-inch, 4H-SiC [0001], n-type epi wafer with 4° off-orientation toward the $[11\bar{2}0]$ direction. The thickness of the epitaxial film was 10 μm. The surface morphology of the entire epitaxial wafer was investigated, and a carrot defect with a shallow pit on the upstream side was detected using MPJ inspection. The surface morphology of the carrot defect was investigated using MPJ and scanning electron microscopy (SEM) at an accelerating voltage of 2 kV (Helios660; Thermo Fisher Scientific). Cross-sectional and plan-view observations of the conversion point of the carrot defect were performed using TEM at an accelerating voltage of 300 kV (H9000; Hitachi High-Technologies).

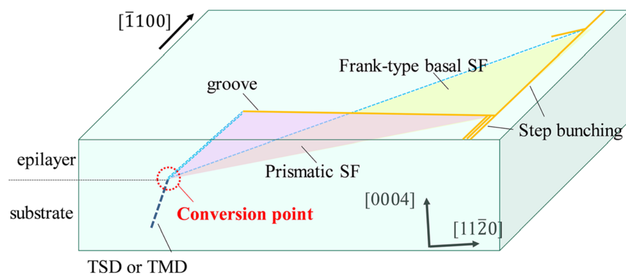

Fig. 1. Schematic illustration of a carrot defect.

Characterization of the atomic structure of the origin was performed using spherical-aberration-corrected STEM at accelerating voltage of 200 kV (ARM200F; JEOL Ltd.). A focused ion beam system (FB2100: Hitachi High-Technologies) was employed for specimen preparation for TEM and STEM observations.

RESULTS AND DISCUSSION

The surface morphology of an entire epi wafer was investigated using MPJ to classify extended defects in the epi layer. Figure 2a shows an MPJ image of one of the carrot defects detected in the above inspection. MPJ can visualize the slight changes in potential due to the surface morphology, local charging, and crystal defects existing beneath the epitaxial film surface.[6,7] From the contrast variations in MPJ images, the carrot defect had one groove almost parallel to the $[11\bar{2}0]$ direction. The groove arose from the surface roughness due to the PSFs. In addition, the line contrast with an angle of about 30° to the $[11\bar{2}0]$ direction is due to the Frank-type partial dislocations. The pit caused by a threading dislocation can be observed at the upstream side of the carrot defect in the MPJ image. The pit cannot be detected in the SEM image shown in Fig. 2b of the same area corresponding to the above MPJ image at the same magnification. However, the pit can be observed in the enlarged SEM image shown in Fig. 2c. The position of the pit corresponds to the point of intersection of the two lines, the extension lines of the groove and the line contrast to the upstream side. Hence, the conversion point at the interface between the epitaxial layer and the substrate is assumed to be beneath the pit. Figure 3 shows the cross-sectional TEM images beneath the pit taken along the $[\bar{1}100]$

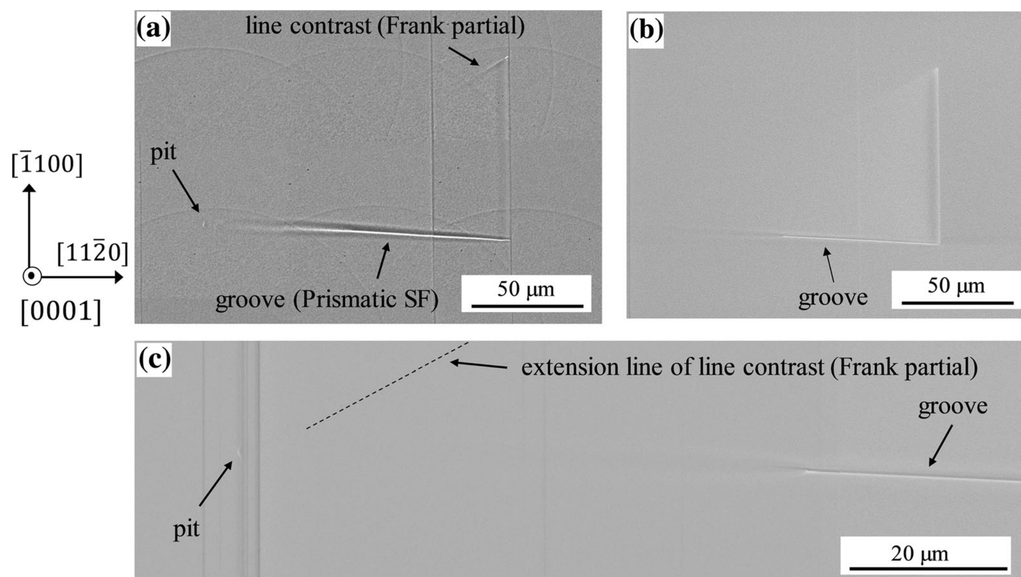

Fig. 2. (a) MPJ image and (b, c) SEM images of the carrot defect on the 4H-SiC epitaxial wafer surface.

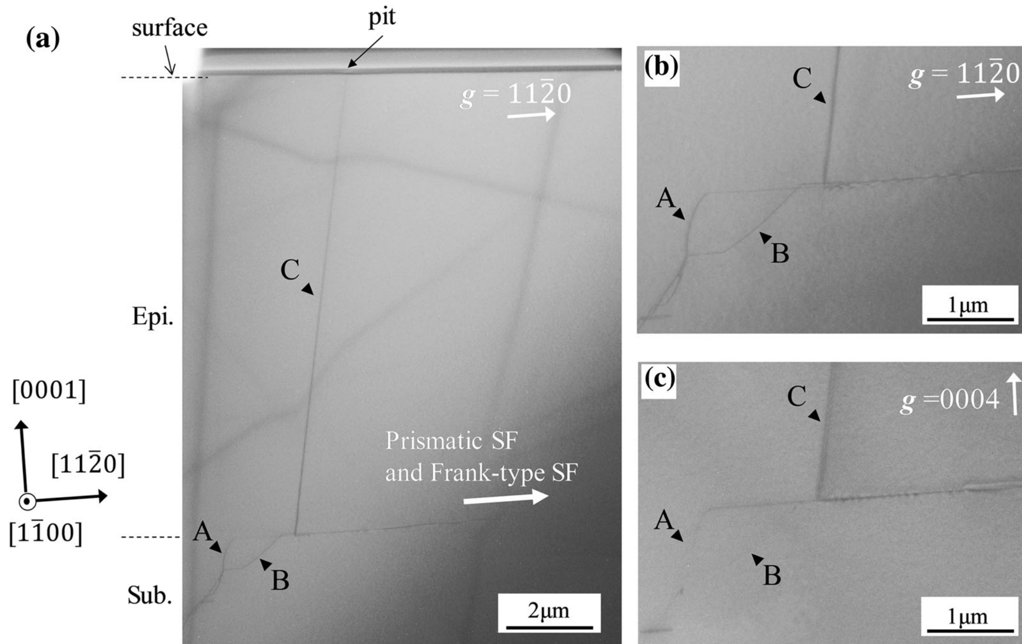

Fig. 3. Cross-sectional TEM images beneath the pit of the carrot defect under two diffraction conditions; (a, b) $\boldsymbol{g} = 11\bar{2}0$ and (c) $\boldsymbol{g} = 0004$. [Under the $\boldsymbol{g} = 11\bar{2}0$ condition, the TEM observation direction is not parallel to the basal plane (0001). Therefore, the two dislocations seem to be lying on different basal planes, even though they are on the same basal plane.].

direction. The interface between the epitaxial layer and the substrate was determined from the SEM contrast modulation of the cross section near the carrot defect. Two dislocations can be observed in the substrate, indicated as triangle A and B in Fig. 3a. The two dislocations propagate on the basal plane at the interface between the epitaxial layer and the substrate, and lead to the generation of a threading dislocation indicated as triangle C in Fig. 3a and a carrot defect that consists of a PSF and a Frank-type SF. Figure 3b and c show TEM images taken under $\boldsymbol{g} = \left[11\bar{2}0\right]$ and $\boldsymbol{g} = 0004$, respectively. The contrast of the dislocations in the TEM images depends on the scalar product $\boldsymbol{g}\cdot\boldsymbol{b}$, where $\boldsymbol{g}$ and $\boldsymbol{b}$ are the diffraction vector and Burgers vector for the dislocations, respectively. When the direction of $\boldsymbol{g}$ is parallel to $\boldsymbol{b}$, the contrast is emphasized, while when $\boldsymbol{g}$ is perpendicular to $\boldsymbol{b}$, the contrast due to the dislocations disappears (hereinafter, this method is called "$\boldsymbol{g}\cdot\boldsymbol{b}$ analysis"). The contrasts of dislocations A and B disappear under the condition $\boldsymbol{g} = 0004$. This result indicates that the Burgers vectors for dislocations A and B lie on the basal plane. On the other hand, the contrast of threading dislocation C running to the epi surface is present under both diffraction conditions. Therefore, the Burgers vector of the threading dislocation C was presumed to have multiple components, such as that of TMD.[8] From these results, the two threading edge dislocations (TEDs) in the substrate are the origin of the carrot defect. The two TEDs were converted to two basal plane dislocations (BPDs) at the interface between the epitaxial layer and the substrate. The two BPDs subsequently led to the generation of the TMD and the carrot defect. In addition to TSDs and TMDs, TEDs are also considered to have the potential to generate carrot defects.

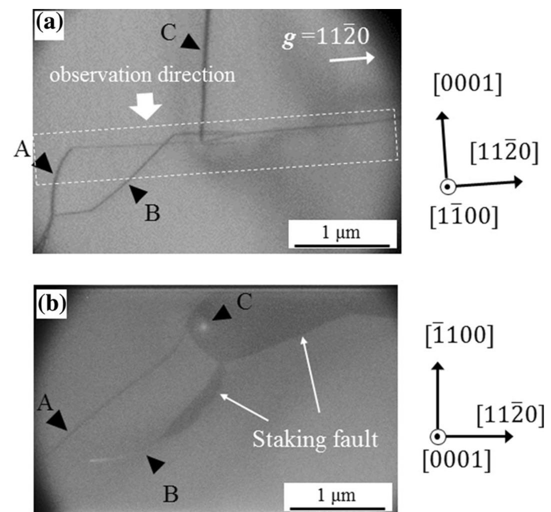

Fig. 4. (a) Cross-sectional TEM image under $\boldsymbol{g} = 11\bar{2}0$ and (b) plan-view TEM image of the conversion point. [Under the $\boldsymbol{g} = 11\bar{2}0$ condition, the TEM observation direction is not parallel to the basal plane (0001). Therefore, the two dislocations seem to be lying on different basal planes, even though they are on the same basal plane.].

In addition, plan-view TEM observations were performed to analyze the detailed structure of the conversion point. The sampling area and direction of observation of the plan-view TEM are shown in the TEM image in Fig. 4a. Figure 4b shows the

Fig. 5. (a–f) Plan-view TEM images under various diffraction conditions and (g) schematic of the conversion point.

Fig. 6. (a) Cross-sectional position and direction of STEM observation, (b) atomic-resolution HAADF-STEM image of dislocation A taken along the $[\bar{1}2\bar{1}0]$ direction, and (c) schematic stacking structure around dislocation A.

Fig. 7. (a) Cross-sectional position and direction of STEM observation, (b, d) HAADF-STEM images of the partials of dislocation B taken along the $[\bar{1}2\bar{1}0]$ direction, and (c, e) schematic stacking structures around the partials of dislocation B.

plan-view TEM image of the conversion point taken along the [0001] direction. The dark contrast areas in the TEM image are the stacking faults. The result indicates that dislocation B is dissociated into two partial dislocations, which are accompanied by the stacking fault, at the interface between the epilayer and the substrate. Figure 5a–f shows plan-view TEM images of the conversion point under different diffraction conditions ($\boldsymbol{g}$ = $[11\bar{2}0]$, $1\bar{2}10$, $\bar{2}110$, $1\bar{1}00$, $\bar{1}010$, and $01\bar{1}0$). The TEM image in Fig. 5c confirms that dislocation A led to the generation of threading dislocation C running to the epi surface and four partial dislocations on the basal plane, indicated as triangles D, E, F, and G. This is similar to the case of simultaneous generation of a TSD (or TMD) and a Frank-type SF, reported by Tsuchida et al.[9] Because the Burgers vector of a TED has no c-component such as $\boldsymbol{b}$ = [0001], the c-component of the Burgers vector of threading dislocation C may be opposite in sign to the sum of those of the four partial dislocations. In addition, dislocation B joined one of the four partial dislocations, G, at the interface, and the merged dislocation was assumed to cause the formation of the PSF. From the results of the $\boldsymbol{g}\cdot\boldsymbol{b}$ analyses in Fig. 5a–f, dislocation A has a Burgers vector of $\boldsymbol{b} = (\pm 1/3)[\bar{2}110]$ because the contrast of A disappeared when $\boldsymbol{g}$ = $01\bar{1}0$ in Fig. 5f. In contrast, the perfect segment and two partial segments with the stacking fault of dislocation B disappeared when $\boldsymbol{g}$ = $1\bar{1}00$, $1\bar{2}10$, and $\bar{2}110$, respectively. The results indicate that the Burgers vector for dislocation B is $\boldsymbol{b} = (\pm 1/3)[11\bar{2}0] = (\pm 1/3)[10\bar{1}0] + (\pm 1/3)[01\bar{1}0]$. The Burgers vectors for dislocations C, D, E, F, and G could not be determined precisely in this study.

High-resolution STEM observations were used to determine the signs of the Burgers vectors for dislocations A and B by using the finish-to-start right-hand convention.[10] Figure 6b shows an atomic-resolution high-angle annular dark-field (HAADF) STEM image of dislocation A. The STEM images were captured along the $[\bar{1}2\bar{1}0]$ zone axis at the position shown in Fig. 6a, and the direction of dislocation was considered to be perpendicular to the plane of the image. A Burgers circuit was drawn

around dislocation A, which is shown as the yellow arrow in the STEM image in Fig. 6b. Figure 6c shows the same Burgers circuit drawn on a perfect 4H-structure matrix. The vector required to close the lattice circuit drawn from the finish point F to the start point S is defined as the Burgers vector. As a result, the Burgers vector of dislocation A was determined to be $\boldsymbol{b} = 1/3[\bar{2}110]$. Figure 7b and d shows cross-section HAADF-STEM images of the two partial segments of dislocation B. The STEM images were captured along the $[\bar{1}2\bar{1}0]$ zone axis at the position shown in Fig. 7a, and the directions of dislocations were considered to be perpendicular to the plane of the image. Similar to the case of dislocation A, Burgers circuits were drawn around the two partial dislocations, which are shown as yellow arrows in the STEM images in Fig. 7b and d. Figure 7c and e shows the same Burgers circuits drawn on a perfect 4H-structure matrix. These results indicate that the Burgers vectors for the two partial dislocations are $\boldsymbol{b} = 1/3[0\bar{1}10]$ and $\boldsymbol{b} = 1/3[\bar{1}010]$, respectively. Therefore, the Burgers vectors for dislocation B were determined to be $\boldsymbol{b} = 1/3[\bar{1}\bar{1}20]$. Consequently, the two dislocations, which are the origin of the carrot defect, are the two TEDs with $\boldsymbol{b} = 1/3[\bar{2}110]$ and $\boldsymbol{b} = 1/3[\bar{1}\bar{1}20]$.

CONCLUSIONS

A carrot defect with a shallow pit was detected in a 4H-SiC epitaxial wafer by using MPJ inspection. The origin and microstructure of the conversion point of the carrot defect were investigated using TEM and high-resolution STEM. We found that two types of TEDs with $\boldsymbol{b} = 1/3[\bar{2}110]$ and $\boldsymbol{b} = 1/3[\bar{1}\bar{1}20]$ in the substrate can generate the carrot defect with a shallow pit in the epitaxial layer. The conversion point was located beneath the pit observed at the upstream side of the carrot defect. The two dislocations were converted to BPDs at the conversion point. Furthermore, one of the two BPDs led to the pair generation of a threading dislocation running to the epi surface and four partial dislocations on the basal plane. The other BPD joined one of the four partial dislocations at the interface; this merged dislocation was assumed to cause the formation of the PSF. Consequently, these dislocations were assumed to generate the carrot defect with a shallow pit in the epitaxial layer. We could not find carrot defects showing similar surface morphology with a shallow pit as reported in this study. Though we could not characterize the microstructure of all the carrot defects in the wafer, we assumed that the carrot defect we reported occurs very rarely. However, to improve the reliability and yield of SiC devices and to reduce the density of carrot defects, the density of not only TSDs and TMDs but also TEDs must be reduced.

CONFLICT OF INTEREST

The authors declare that they have no conflicts of interest.

REFERENCES

1. H. Matsunami and T. Kimoto, *Mater. Sci. Eng. R* 20, 125 (1997).
2. E. Van Brunt, A. Burk, D.J. Lichtenwalner, R. Leonard, S. Sabri, D.A. Gajewski, A. Mackenzie, B.A. Hull, S. Allen, and J.W. Palmour, *Mater. Sci. Forum* 924, 137 (2017).
3. M. Benamara, X. Zhang, M. Skowronski, P. Ruterana, G. Nouet, J.J. Sumakeris, M.J. Paisley, and M.J. O'Loughlin, *Appl. Phys. Lett.* 86, 021905 (2005).
4. H. Tsuchida, M. Ito, I. Kamata, and M. Nagano, *Phys. Status Solidi B* 246, 1553 (2009).
5. J. Hassan, A. Henry, P.J. McNally, and J.P. Bergman, *J. Cryst. Growth* 312, 1828 (2010).
6. M. Hasegawa and T. Shimakura, *J. Appl. Phys.* 107, 084107 (2010).
7. M. Hasegawa and T. Ohno, *J. Appl. Phys.* 110, 073507 (2011).
8. J. Guo, Y. Yang, F. Wu, J.J. Sumakeris, L.T. Leonard, O. Goue, B. Raghothamachar, and M. Dudley, *Mater. Sci. Forum* 858, 15 (2016).
9. H. Tsuchida, I. Kamata, and M. Nagano, *J. Cryst. Growth* 310, 757 (2008).
10. J.P. Hirth and J. Lothe, *Theory of Dislocations* (Malabar: Krieger, 1992), pp. 17–20.

Publisher's Note Springer Nature remains neutral with regard to jurisdictional claims in published maps and institutional affiliations.